

# Uniform Alkaline Earth Fluoride Nanocrystals with Diverse Shapes Grown from Thermolysis of Metal Trifluoroacetates in Hot Surfactant Solutions

Ya-Ping Du, Xiao Sun, Ya-Wen Zhang,\* Zheng-Guang Yan, Ling-Dong Sun, and Chun-Hua Yan\*

Beijing National Laboratory for Molecular Sciences, State Key Laboratory of Rare Earth Materials Chemistry and Applications, PKU-HKU Joint Laboratory in Rare Earth Materials and Bioinorganic Chemistry, Peking University, Beijing 100871, China

Received December 17, 2008; Revised Manuscript Received January 9, 2009

**ABSTRACT:** Uniform alkaline earth metal fluoride  $\text{MF}_2$  ( $\text{M} = \text{Mg}$ ,  $\text{Ca}$ , and  $\text{Sr}$ ) nanocrystals with various shapes (tetragonal  $\text{MgF}_2$  nanoneedle-constructed 3D networks; cubic  $\text{CaF}_2$  nanoplates and nanopolyhedra; cubic  $\text{SrF}_2$  nanoplates and nanowires) have been synthesized from the thermolysis of alkaline earth metal trifluoroacetate ( $\text{M}(\text{CF}_3\text{COO})_2$ ) in hot surfactant solutions (oleic acid, oleylamine, and 1-octadecene). The  $\text{MF}_2$  nanocrystals were formed by the controlled fluorination of the  $\text{M}-\text{O}$  bond into the  $\text{M}-\text{F}$  bond at the nucleation stage and subsequent growth process. For phase-pure  $\text{MF}_2$  nanocrystals, the growth of shape-selective  $\text{MF}_2$  nanocrystals was likely due to the template direction of micellar structures formed by self-assembly of capping ligands and the so-called “Ostwald ripening” process. With the developed synthetic strategy, the uniform upconversion  $\text{SrF}_2:\text{Yb,Er}$  and core/shell  $\text{SrF}_2:\text{Yb,Er}@\text{SrF}_2$  nanocrystals were also obtained. The core/shell-structured nanocrystals exhibited enhanced emission intensity and saturation power with respect to their core counterparts, owing to the suppression of associated nonradiative decays.

## Introduction

Fluoride materials have been investigated for ages because they have diverse optical applications owing to their low-energy phonons and high ionicity, which lead to the lower quenching probability of the excited states with respect to other materials, such as oxides or sulfides.<sup>1</sup> As an important family of fluorides, alkaline earth metal fluorides  $\text{MF}_2$  ( $\text{M} = \text{Mg}$ ,  $\text{Ca}$ ,  $\text{Sr}$ , and  $\text{Ba}$ ) with unique luminescent, insulating, and electric properties have drawn tremendous attention.<sup>2</sup> It is widely accepted that the actualization of nanosized materials has opened doors for finding new properties with respect to their macroscopic counterparts. As a consequence, it is reasonably believed that with the development of nanometer materials, the unique physical and chemical properties of fluorides nanomaterials could definitely captivate the material world with the promise of exciting applications in science and technology.<sup>3</sup>

There are some reports on the synthesis of  $\text{MF}_2$  nanomaterials with limited wet chemical approaches involving modified coprecipitation, reversed micelle, and hydrothermal methods.<sup>4</sup> For instance, size-controllable  $\text{CaF}_2$  nanocubes have been obtained by using a hydrothermal method in the absence of surfactants.<sup>4a</sup> One-dimensional (1D)  $\text{BaF}_2$  nanowhiskers and single-crystal nanorods have been fabricated with a microemulsion-mediated hydrothermal method.<sup>4b</sup> Nanocrystalline  $\text{CaF}_2$  has been made by a polyol method using diethylene glycol (DEG) as a solvent.<sup>4d</sup> Single-crystal  $\text{BaF}_2$  nanocubes with controllable size from 10 to 1000 nm have been prepared using a hydrothermal precipitation procedure in the presence of selenite ions.<sup>4e</sup> However, to date, most developed synthetic methods available for  $\text{MF}_2$  nanocrystals are substantially based on the precipitation reaction between soluble alkaline earth metal salts and alkali fluorides, and the synthesis of high-quality (monodisperse, single-crystalline, well-shaped, and phase-pure) dispersible  $\text{MF}_2$  nanocrystals has rarely been reported.<sup>4f,g</sup> Therefore, it still

remains a challenge to establish a new synthetic route toward a general synthesis of high-quality  $\text{MF}_2$  nanocrystals.

In this article, we present a controlled synthesis of uniform alkaline earth metal fluoride  $\text{MF}_2$  (here,  $\text{M} = \text{Mg}$ ,  $\text{Ca}$ , and  $\text{Sr}$ ) nanocrystals with diverse shapes through the thermolysis of  $\text{M}(\text{CF}_3\text{COO})_2$  in hot surfactant solutions (oleic acid, oleylamine, and 1-octadecene). We prepared the tetragonal  $\text{MgF}_2$  nanoneedle-constructed 3D networks, cubic  $\text{CaF}_2$  nanoplates and nanopolyhedra, cubic  $\text{SrF}_2$  nanoplates, and nanowires by controlling the fluorination of alkaline earth metal in the solution. We found that growth of the shape-selective  $\text{MF}_2$  nanocrystals was likely induced by tunable templating interactions from the micelle-like structure formed by the self-organization of capping ligands. With this developed synthetic strategy, we also obtained the uniform  $\text{SrF}_2:\text{Yb,Er}$  and core/shell-structured  $\text{SrF}_2:\text{Yb,Er}@\text{SrF}_2$  nanocrystals, which showed interesting upconversion properties.

## Experimental Section

**1. Chemicals.** Oleic acid (OA; 90%, Alpha), oleylamine (OM; >80%, Acros), 1-octadecene (ODE; >90%, Acros), absolute ethanol, and cyclohexane were used as received.  $\text{M}(\text{CF}_3\text{COO})_2$  precursors were prepared by the literature method,<sup>5</sup> using alkaline earth metals salts (>99.95%) and trifluoroacetic acid (99%, Acros) as the starting materials.

**2. Nanocrystal Synthesis. 2.1. Synthesis of  $\text{MF}_2$  Nanocrystals.** The synthesis was carried out using the standard oxygen-free procedures. A typical procedure was described as follows: a given amount of  $\text{M}(\text{CF}_3\text{COO})_2$  (1 mmol) was added into 40 mmol of OA/OM/ODE in a three-necked flask (100 mL) at room temperature. Then, the slurry was heated to 100 °C to remove water and oxygen with vigorous magnetic stirring under vacuum for several minutes in a temperature-controlled electromantle and thus to form an optically transparent solution. The solution was then heated to a temperature within 250–320 °C at a heating rate of 20 °C/min and kept for 1 h under an inert Ar atmosphere. On cooling to room temperature, the nanocrystals were precipitated by adding an excess amount of ethanol into the reacted solution, followed by washing with ethanol and drying in an oven at 70 °C. The as-prepared dried nanocrystals could be easily dispersed in

\* To whom correspondence should be addressed. Fax: +86-10-6275 4179. E-mail: yan@pku.edu.cn, ywzhang@pku.edu.cn.

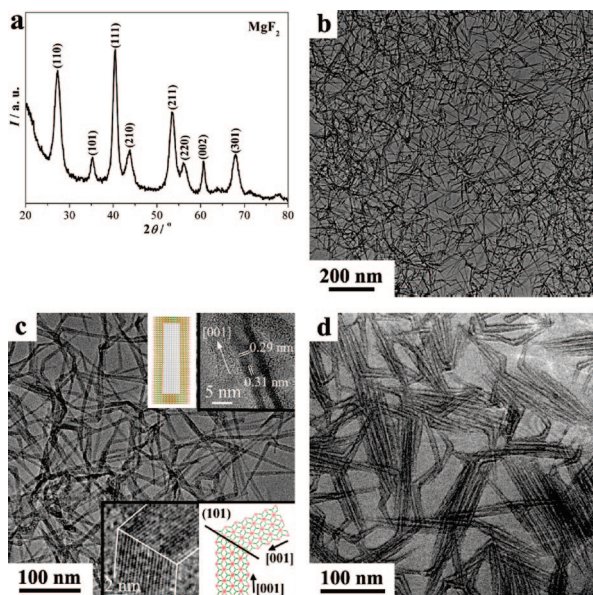


**Figure 1.** XRD pattern (a) and TEM and HRTEM images (inset) of the  $\text{MgF}_2$  nanoneedle-constructed 3D networks with (b) low and (c) high magnifications. (Inset, c) Bottom right, twin structures with the model. (d) TEM image of the  $\text{MgF}_2$  nanoneedle-constructed network taken at an electron beam exposure time of 30 s.

various nonpolar organic solvents such as cyclohexane. The yields of all the obtained nanocrystals were about 50–70%.

**2.2. Synthesis of  $\text{SrF}_2$ :20%Yb,2%Er Nanocrystals.** The synthetic procedure was similar to that of  $\text{SrF}_2$  nanocrystals, except that 0.78 mmol of  $\text{Sr}(\text{CF}_3\text{COO})_2$ , 0.20 mmol of  $\text{Yb}(\text{CF}_3\text{COO})_3$ , and 0.02 mmol of  $\text{Er}(\text{CF}_3\text{COO})_3$  were taken as the precursors and added into a mixture of OA (20 mmol) and ODE (20 mmol) in a three-necked flask at room temperature for a reaction at 280–300 °C for 30–60 min.

**2.3. Synthesis of  $\text{SrF}_2$ :20%Yb,2%Er@ $\text{SrF}_2$  Nanocrystals.** The synthetic procedure was the same as that used to synthesize  $\text{SrF}_2$ :20%Yb,2%Er nanocrystals, except that 1 mmol of the above-prepared  $\text{SrF}_2$ :20%Yb,2%Er nanocrystals and 1 mmol of  $\text{Sr}(\text{CF}_3\text{COO})_2$  were taken as the precursors and were added into a mixture of OA (20 mmol) and ODE (20 mmol) in a three-necked flask at room temperature.

**3. Instrumentation.** The X-ray diffraction (XRD) patterns were recorded on a Rigaku D/MAX-2000 (Japan) diffractometer with a slit of  $1/2^\circ$  at a scanning rate of  $4^\circ \text{ min}^{-1}$ , using  $\text{Cu K}\alpha$  radiation ( $\lambda = 1.5418 \text{ \AA}$ ). Samples for XRD analysis were prepared by drying the nanocrystals in an oven at 70 °C for 12 h. The lattice parameters were calculated using the least-squares method.<sup>6</sup> TEM images were acquired by a JEOL 200CX transmission electron microscope (TEM, Japan) operating at 160 kV. High-resolution TEM (HRTEM) micrographs were obtained with a Philips Tecnai F30 FEG-TEM (The Netherlands) operated at 300 kV. Samples for TEM and HRTEM analysis were prepared by drying a dispersion of the nanocrystals on amorphous carbon-coated copper grids. The room-temperature upconversion emission spectra of lanthanide-doped  $\text{SrF}_2$  nanocrystals were measured on a modified Hitachi F-4500 spectrophotometer (Japan) with an external tunable 2 W 980 nm laser diode as the excitation source, with the suspensions of the dried nanocrystal powder redispersed in the mixture of toluene/hexane (v/v = 1:1) at the calculated concentration of around  $0.05 \text{ mol} \cdot \text{L}^{-1}$ .

## Results and Discussion

### 1. Characterization of $\text{MF}_2$ (M = Mg–Ba) Nanocrystals.

**1.1. Tetragonal  $\text{MgF}_2$  Nanocrystals.** The XRD pattern shown in Figure 1a reveals that the as-obtained  $\text{MgF}_2$  nanocrystals are characteristic of a pure tetragonal phase (space group  $P4_2/mnm$ ). The calculated lattice constants are  $a = 4.621 \text{ \AA}$  and  $c = 3.046 \text{ \AA}$  for  $\text{MgF}_2$  (JCPDS 41-1443). The broadening of diffraction peaks indicates the nanocrystalline nature of this sample.

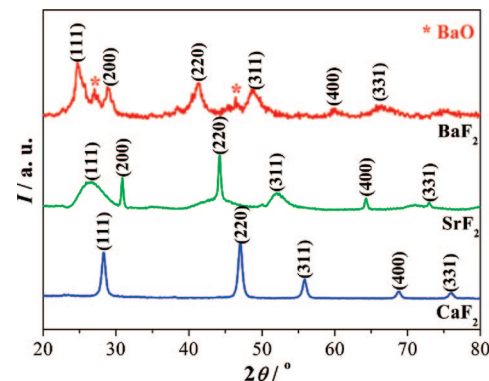


**Figure 2.** XRD patterns of cubic  $\text{MF}_2$  (M = Ca, Sr, Ba) nanocrystals.

TEM characterization has demonstrated that the as-obtained tetragonal  $\text{MgF}_2$  exhibit a three-dimensional (3D) network-like nanostructure consisting of needle-shaped nanocrystals with relatively high aspect ratios. Figure 1b depicts the TEM image of  $(13.2 \pm 1.7) \text{ nm} \times (80\text{--}170) \text{ nm}$   $\text{MgF}_2$  nanoneedle-constructed 3D networks redispersed in cyclohexane. For more distinct observation, a higher magnification TEM image is shown in Figure 1c, from which a large amount of sharp corners was found in the as-prepared bended  $\text{MgF}_2$  networks. Interestingly, as disclosed by HRTEM images inserted in Figure 1c, the sharp corners exhibited characteristics of twinned crystals (lower inset), and such a nanoneedle is composed of one to three single-crystalline nanoneedles network connected with the twinned crystals. The  $\text{MgF}_2$  nanoneedles spanning the network show a preferred growth direction along the  $\langle 001 \rangle$  direction, and interplanar distances of 0.29 nm ascribed to the  $\langle 001 \rangle$  facet and 0.31 nm attributable to the  $\langle 110 \rangle$  facet are observed (upper inset in Figure 1c). It is also noted that the as-obtained  $\text{MgF}_2$  nanoneedle-constructed 3D networks are rather unstable and can be easily converted to the tube-like structure under the irradiation of the electron beam (Figure 1d), perhaps owing to the light atomic weight of magnesium and high-energy beam of the electron microscope.<sup>7</sup>

**1.2. Cubic  $\text{MF}_2$  (M = Ca, Sr, Ba) Nanocrystals.** The XRD patterns shown in Figure 2 showed the cubic phase for the obtained  $\text{MF}_2$  (space group  $Fm\bar{3}m$ ) nanocrystals. The calculated lattice constants are as follows:  $a = 5.460 \text{ \AA}$  for  $\text{CaF}_2$  (JCPDS 35-0816),  $a = 5.791 \text{ \AA}$  for  $\text{SrF}_2$  (JCPDS 06-0262), and  $a = 6.180 \text{ \AA}$  for  $\text{BaF}_2$  (JCPDS 04-0452). The broadening of the reflections ascribed to the  $\text{CaF}_2$  and  $\text{SrF}_2$  samples obviously signifies their nanocrystalline nature, and the  $\text{BaF}_2$  sample also contains the impurity of BaO. Noticeably, the XRD profile for  $\text{SrF}_2$  appears conspicuously with some reflections of preferred orientations, i.e., the sharp peaks for  $\langle 200 \rangle$  and  $\langle 220 \rangle$  planes, whereas the broadened ones for others, which indicates a relatively big size along the  $\langle 200 \rangle$  and  $\langle 220 \rangle$  directions for the as-obtained  $\text{SrF}_2$  nanocrystals.

TEM characterization has demonstrated that the as-obtained cubic  $\text{MF}_2$  nanocrystals take on a plate-like shape in most cases, and the length-to-width aspect ratios of most nanocrystals are less than 2. The TEM image shown in Figure 3a has disclosed that the as-synthesized cubic  $\text{CaF}_2$  nanocrystals display a quadrilateral plate shape in the size of  $(33.1 \pm 5.9) \text{ nm} \times (45.5 \pm 5.6) \text{ nm}$ . The inset in Figure 3a is the typical HRTEM image of  $\text{CaF}_2$  nanocrystals that displays evident lattice fringes, indicating the high crystallinity of the as-obtained nanocrystals. The interplanar spacings for the  $\text{CaF}_2$  nanocrystals are calculated



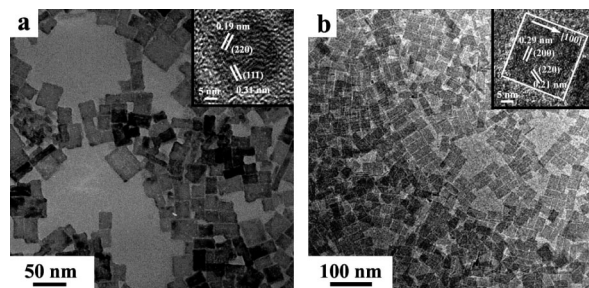


**Figure 3.** TEM and HRTEM (inset) images of (a)  $\text{CaF}_2$  nanoplates and (b)  $\text{SrF}_2$  nanoplates.

to be 0.31 and 0.19 nm, identical to the distances of the (111) and (220) facets of bulk  $\text{CaF}_2$ , respectively.

Under the same synthetic conditions as those used for preparing uniform  $\text{CaF}_2$  nanocrystals (Table 1), we also obtained high-quality  $\text{SrF}_2$  nanoplates. Figure 3b shows the TEM image of the  $\text{SrF}_2$  nanocrystals with a size of  $(36.4 \pm 3.3) \text{ nm} \times (25.1 \pm 1.8) \text{ nm}$  in the top surface. The typical HRTEM image inserted in Figure 3b demonstrates that the  $\text{SrF}_2$  nanocrystals are single crystalline, and the interplane distance of the lattice fringes is about 0.21 and 0.29 nm, which correspond to that of the (220) and (200) facets of  $\text{SrF}_2$ , respectively. This result is in agreement with the XRD measurements (Figure 2). Meanwhile, the uniform  $\text{SrF}_2$  nanoplates can spontaneously assemble into two-dimensional (2D) patterns in a short range, indicative of the presence of capping ligands on the surfaces of nanocrystals.<sup>8</sup>

However, for  $\text{BaF}_2$  sample, they only present large nonuniform  $\text{BaF}_2$  microsquares with a size of  $1 \mu\text{m} \times 1 \mu\text{m}$  and separated  $\text{BaO}$  nanoparticles, and these microcrystals could not be well dispersed in the current dispersant (Figure S1 in the Supporting Information). The average sizes of nanocrystals are estimated by Scherrer's formula:  $D_{hkl} = K\lambda/\beta \cos \theta$ , where  $\lambda$  is the X-ray wavelength ( $\lambda = 1.5405 \text{ \AA}$ ),  $\beta$  is the full width at half-maximum,  $\theta$  is the diffraction angle,  $K$  is a constant (0.89), and  $D_{hkl}$  means the size along the ( $hkl$ ) direction. The estimated average crystallite sizes are 12.7 ( $\text{MgF}_2$ ), 32.1 ( $\text{CaF}_2$ ), and 34.1 nm ( $\text{SrF}_2$ ), which agree well with those observed from TEM images. In addition, the atomic ratios of metals in the nanocrystals are determined by energy-dispersive X-ray analysis (EDAX, which was detected in three different areas of the TEM copper grid), showing that the atomic ratios of F to M ( $M = \text{Mg}-\text{Ba}$ ) are in agreement with the expected values, thus confirming the formation of stoichiometric  $\text{MF}_2$  compounds (Figure S2 in the Supporting Information).

## 2. Optimized Reaction Parameters for $\text{MF}_2$ Nanocrystals.

**2.1. Concentration of the Precursor.** In the current research, proper monomer concentrations play an important role in the formation of high-quality  $\text{MF}_2$  nanocrystals. For example, fixing the volume of solvents, when using 1 mmol of  $\text{Mg}(\text{CF}_3\text{COO})_2$  in  $\text{OA}/\text{ODE} = 1:1$  for a reaction at  $280^\circ\text{C}$  for 60 min, we obtained well-separated and dispersed zigzag-shaped  $\text{MgF}_2$  nanoneedle-constructed networks in the size of  $(8.2 \pm 0.4) \text{ nm} \times (50-90) \text{ nm}$  but with low yield (Figure S3a in the Supporting Information). Under the same reaction condition, except increasing  $\text{Mg}(\text{CF}_3\text{COO})_2$  concentration to 2 mmol resulted in  $\text{MgF}_2$  nanoneedle-constructed networks in the size of  $(10.5 \pm 0.4) \text{ nm} \times (58-100) \text{ nm}$  with enhanced yield and good dispersibility (Figure S3b in the Supporting Information), while further increasing  $\text{Mg}(\text{CF}_3\text{COO})_2$  concentration to 4 mmol produced aggregated ones  $((11.5 \pm 1.4) \text{ nm} \times (44-138) \text{ nm})$  with poor dispersibility (Figure S3c in the Supporting Information). As

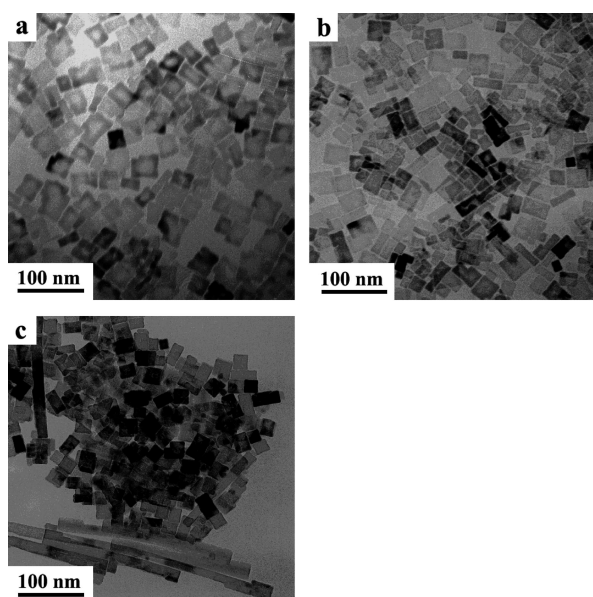
the case for  $\text{CaF}_2$  nanoplates, by using different concentrations of precursor under the fixed reaction temperature ( $280^\circ\text{C}$ ) and time (60 min) in the mixed solvent  $\text{OA}/\text{ODE} (1:1)$ , we got the different shaped  $\text{CaF}_2$  nanocrystals. If compared with the nanocrystals synthesized using 1 mmol of  $\text{Ca}(\text{CF}_3\text{COO})_2$  (Figure 4a,  $(31.1 \pm 3.3) \text{ nm} \times (42.1 \pm 3.6) \text{ nm}$ ), the dissolution of nanoplates' centers was obviously restrained when adopting the 1.5 mmol precursor (Figure 4b,  $(33.2 \pm 5.0) \text{ nm} \times (44.7 \pm 4.2) \text{ nm}$ ). With increasing the  $\text{Ca}(\text{CF}_3\text{COO})_2$  concentration to 2 mmol, the well-defined rectangle-plate shaped nanocrystals were harvested (Figure 3a), and the nanocrystals were of nearly cubic shape in the size of  $(26.7 \pm 3.2) \text{ nm} \times (28.6 \pm 3.8) \text{ nm}$ . When further increasing the  $\text{Ca}(\text{CF}_3\text{COO})_2$  concentration up to 4 mmol (Figure 4c), cubes coexisted with a few nanorods with a length of ca. 300 nm were formed for  $\text{CaF}_2$ . To conclude, the molar ratio of precursor to solvent (40 mmol) ranging from 1:10 to 1:60 is proper for the preparation of uniform  $\text{MF}_2$  nanocrystals.

**2.2. Solvent Composition.** It seems that the use of a mixed solvent of  $\text{OA}/\text{OM}/\text{ODE}$  is essential for the preparation of phase-pure and uniform  $\text{MF}_2$  nanocrystals. For instance, for the synthesis of  $\text{CaF}_2$  nanocrystals, in pure  $\text{OA}$ , only dispersed but nonuniform  $\text{CaF}_2$  nanoplates  $((12.0 \pm 3.3) \text{ nm} \times (13.2-38.8) \text{ nm})$  were obtained (Figure 5a). In pure  $\text{OM}$ , the dispersible and uniform  $\text{CaF}_2$  nanocrystals  $(10.8 \pm 0.2) \text{ nm}$  were produced (Figure 5b), while in pure  $\text{ODE}$ , the separated solid matters containing severely aggregated  $\text{CaF}_2$  products (Figure 5c) were observed. The above case was also similar to the synthesis of  $\text{SrF}_2$  nanocrystals. Furthermore, by changing the solvent composition, such as  $\text{OA}/\text{ODE} = 1:3$ , the uniform  $\text{SrF}_2$  nanowires in the size of  $(7.0 \pm 0.3) \text{ nm} \times (80.6 \pm 13) \text{ nm}$  were obtained (Figure 5d). Different from the  $\text{CaF}_2$  and  $\text{SrF}_2$  nanocrystals, as for  $\text{MgF}_2$ , in pure  $\text{OA}$ , the less-aggregated  $\text{MgF}_2$  nanoneedle-constructed networks with the size of  $(8.7 \pm 0.3) \text{ nm} \times (80-160) \text{ nm}$  were obtained (Figure S4a in the Supporting Information). In pure  $\text{ODE}$ , the nondispersible worm-like  $\text{MgF}_2$  nanoparticles were produced (Figure S4b in the Supporting Information). However, the presence of excessive  $\text{OM}$  ligands in the mixed solvent might significantly hinder the growth of  $\text{MgF}_2$  nanocrystals, along with producing nondispersed hexagonal  $\text{Mg}(\text{OH})_2$  (space group  $P-3m1$ ) impurities (Figure S4c,d in the Supporting Information). In summary, the near uniform and phase-pure  $\text{MF}_2$  nanocrystals could be obtained at an optimized  $\text{OA}/\text{OM}/\text{ODE}$  ratio (see Table 1).

**2.3. Reaction Temperature (T) and Time (t).** Besides the solvent composition, we found that both the reaction temperature and time also remarkably affect the quality of the products. For example, under a fixed precursor concentration of 1 mmol of  $\text{Sr}(\text{CF}_3\text{COO})_2$ ,  $\text{OA}/\text{ODE} = 1/1$ , and a reaction time of 1 h, as  $T$  was decreased from 280 to  $260^\circ\text{C}$ , hardly any solid matter appeared after the precipitation treatment, indicating the deficient energy for the decomposition of precursor to form  $\text{SrF}_2$ . As  $T$  was increased to  $300^\circ\text{C}$ , the as-obtained dispersible  $\text{SrF}_2$  nanoplates transform into nanowires with tapered tips, which have the size of  $(3.1 \pm 0.2) \text{ nm} \times (50-120) \text{ nm}$  (Figure 6a). The HRTEM image inserted in Figure 6a demonstrates that the as-obtained  $\text{SrF}_2$  nanowires grow along a preferred  $\langle 001 \rangle$  direction. Further, the elevation of the reaction temperature to  $320^\circ\text{C}$  resulted in nonuniform aggregated  $\text{SrF}_2$  nanocrystals (Figure 6b). Similarly, Figure 7 shows the reaction temperature-dependent shape evolution of  $\text{CaF}_2$  nanocrystal with using 1 mmol of  $\text{Ca}(\text{CF}_3\text{COO})_2$  in  $\text{OA}/\text{ODE} (1:1)$  for 60 min. As the reaction temperature was fixed to  $280^\circ\text{C}$ , the near uniform quadrangular  $\text{CaF}_2$  nanocrystals were formed. Interestingly, the as-obtained nanoplates have the characteristics of thick edges

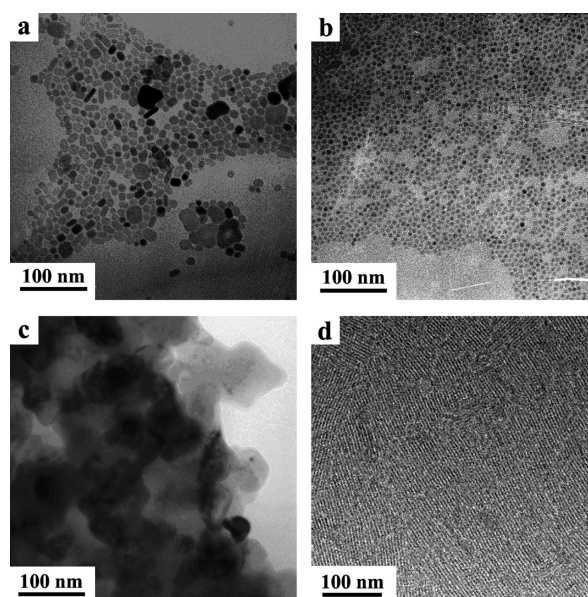
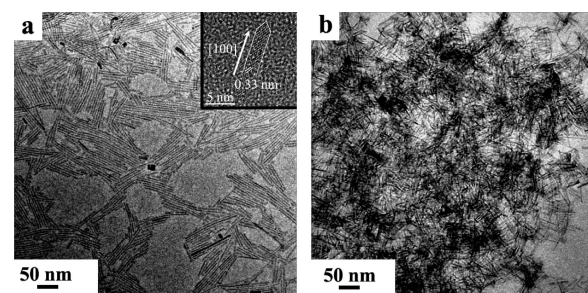
**Table 1.** Crystal Structure, Morphology, and Size of the As-Synthesized MF<sub>2</sub> (M = Mg, Ca, Sr, Ba) Nanocrystals via the Thermolysis of M(CF<sub>3</sub>COO)<sub>2</sub> in Oleic Acid (OA)/Oleylamine (OM)/1-Octadecene (ODE) (40 mmol)<sup>a</sup>

	precursor (mmol)	OA:OM:ODE	T [°C]	t (min)	structure	morphology	size (nm)
MgF <sub>2</sub>	2	1:0:1	300	40	tetragonal	needle network	(13.2 ± 1.7) × (80–170)
	1	1:0:1	280	60	tetragonal	needle network	(8.2 ± 0.4) × (50–90)
	2	1:0:1	280	60	tetragonal	needle network	(10.5 ± 0.4) × (58–100)
	1	0:0:1	280	60	tetragonal	needle network	(8.7 ± 0.3) × (80–160)
	4	1:0:1	280	60	tetragonal	needle network	(11.5 ± 1.4) × (44–138)
CaF <sub>2</sub>	2	1:0:1	280	60	cubic	rectangle	(33.1 ± 5.9) × (45.5 ± 5.6)
	1	1:0:1	280	60	cubic	dual rectangular plate	(31.1 ± 3.3) × (42.1 ± 3.6)
	1	1:0:1	300	60	cubic	dual rectangular plate	(37.2 ± 4.1) × (30.6 ± 3.5)
	1	1:0:1	320	60	cubic	polygon	(30.8 ± 10.0)
	1.5	1:0:1	280	60	cubic	dual rectangular plate	(33.2 ± 5.0) × (44.7 ± 4.2)
	4	1:0:1	280	60	cubic	rectangular and rod	(26.7 ± 3.2) × (28.6 ± 3.8)
	1	1:0:0	280	60	cubic	rectangular	(12.0 ± 3.3) × (13.2–38.8)
	1	0:1:0	280	60	cubic	polyhedron	(10.8 ± 0.2)
SrF <sub>2</sub>	1	1:0:1	280	60	cubic	rectangular	(36.4 ± 3.3) × (25.1 ± 1.8)
	0.25	1:0:3	280	60	cubic	wire	(7.0 ± 0.3) × (80.6 ± 13)
	1	1:0:1	300	60	cubic	wire	(3.1 ± 0.2) × (50–120)
BaF <sub>2</sub>	1	1:0:1	310	60	cubic	microsquare	1000 × 1000

<sup>a</sup> The statistic standard deviation from at least 50 particles.**Figure 4.** TEM images of CaF<sub>2</sub> nanocrystals obtained with different concentrations of Ca(CF<sub>3</sub>COO)<sub>2</sub> in OA/ODE (1:1) at 280 °C for 60 min: (a) 1, (b) 1.5, and (c) 4 mmol.

and thin centers (Figure 4a). When the temperature was raised to 300 °C, the nanostructure with a “dual rectangular” shape was formed ((37.2 ± 4.1) nm × (30.6 ± 3.5) nm), in which the center of nanoquadrangles was hollow (Figure 7a). The HRTEM characterization testified this novel nanostructure was single crystalline (inset of Figure 7a). The hollow structures within nanoscale have become an interesting area;<sup>10</sup> however, to the best of our knowledge, such a dual rectangular-shaped nanocrystal with hollow structure has not been reported in fluorides. The further elevated temperature to 320 °C yielded (30.8 ± 10.0) nm polygonal CaF<sub>2</sub> nanocrystals with a broad size distribution (Figure 7b, SD = 32.5%), meaning a drastic “Ostwald ripening” process proceeds with the increase of reaction temperature.

On the other hand, under the fixed reaction temperature of 300 °C, the thermolysis of 2 mmol of Mg(CF<sub>3</sub>COO)<sub>2</sub> in OA/ODE (1:1) for 5 min results in no tetragonal MgF<sub>2</sub> nanoneedles but some gels (Figure S5a in the Supporting Information). At *t* = 10–15 min, only some unshapely nanoneedle networks coexisted with a great amount of gels (Figure S5b in the

**Figure 5.** TEM images of CaF<sub>2</sub> nanocrystals obtained from the thermolysis of Ca(CF<sub>3</sub>COO)<sub>2</sub> in various solvents: (a) OA, (b) OM, and (c) ODE. (d) TEM image of uniform SrF<sub>2</sub> nanowires synthesized from the thermolysis of 0.25 mmol of Sr(CF<sub>3</sub>COO)<sub>2</sub> under OA/ODE = 1:3 at 280 °C for 60 min.**Figure 6.** TEM and HRTEM (inset) images of SrF<sub>2</sub> nanocrystals obtained from the thermolysis of 1 mmol of Sr(CF<sub>3</sub>COO)<sub>2</sub> in OA/ODE (1:1) for 60 min at different reaction temperatures: (a) 300 and (b) 320 °C.

Supporting Information). When the reaction went on from 20 to 30 min, the nanoneedles were discernible but ill separated (Figure S5c in the Supporting Information). On further extending



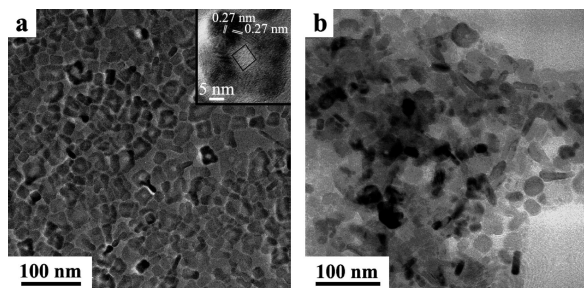
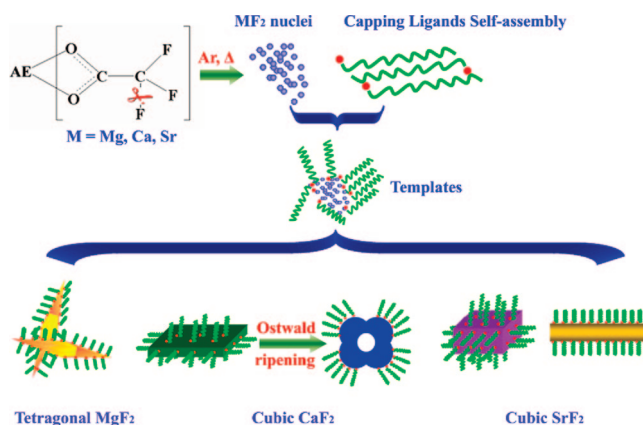


**Figure 7.** TEM and HRTEM (inset) images of  $\text{CaF}_2$  nanocrystals obtained from the thermolysis of 1 mmol of  $\text{Ca}(\text{CF}_3\text{COO})_2$  in OA/ODE (1:1) for 60 min at different reaction temperatures: (a) 300 and (b) 320 °C.

the reaction time to 40 min, well-separated nanoneedle-constructed 3D networks with high aspect ratios were obtained (Figure 1b), indicating a quick “size-focusing” process occurred in the reaction during the time period of  $t = 30\text{--}40$  min. However, as the reaction proceeded for 60 min, aggregated  $\text{MgF}_2$  nanoneedle-contained nonuniform nanoparticles were formed (Figure S5d in the Supporting Information), indicating a distinct “Ostwald ripening” process occurred. Beyond 60 min, the  $\text{MgF}_2$  nanoneedles with a much broader size distribution were again observed (Figure S5e in the Supporting Information), suggesting a drastic “size-defocusing” process appeared at  $t = 40\text{--}60$  min.<sup>9b</sup> As for the cubic  $\text{MF}_2$  ( $M = \text{Ca}, \text{Sr}$ ), the reaction time has also been found significantly influencing the qualities of nanocrystals. For example, Figure S6 in the Supporting Information shows the time-dependent shape evolution of  $\text{SrF}_2$  nanowires synthesized at 300 °C under OA/ODE = 1:1. At  $t = 15$  min, highly aggregated nanowires with low yields were formed (Figure S6a in the Supporting Information). The fast Fourier transform (FFT) analysis inserted in Figure S6a (Supporting Information) testified their poor crystallinity. When the reaction time was prolonged for 30 min, the nanowires were still not well crystallized but were well dispersed (Figure S6b in the Supporting Information; the inset is FFT analysis). At 45 min, well-crystallized but ill-separated nanowires in improved yields were harvested (Figure S6c in the Supporting Information), suggesting a long reaction time enhances the crystallinity of the as-obtained nanocrystals. As the reaction time was extended to 60 min, the as-obtained nanowires display high crystallite size uniformity (Figure 6a). Finally, we found that high-quality  $\text{MF}_2$  ( $\text{Mg}, \text{Ca}, \text{Sr}$ ) nanocrystals can be obtained in an appropriate mixed OA/OM/ODE solvent at higher temperature (280–300 °C) over a longer reaction time (45–60 min) under a relatively low precursor concentration (the molar ratio of precursor to solvent = 1:10–1:60).

**3. Formation of  $\text{MF}_2$  Nanocrystals.** **3.1. Nucleation.** Just like the case of thermolysis of  $\text{RE}(\text{CF}_3\text{COO})_3$  ( $\text{RE} = \text{rare earth}$ ) in mixed solvents of OA/OM/ODE,<sup>8b</sup> as the reaction solution containing  $\text{M}(\text{CF}_3\text{COO})_2$  was rapidly heated to its thermolysis temperature under an Ar atmosphere, tiny gas bubbles evoked from the reaction system instantly, indicating decomposition of the precursor and simultaneous formation of homogeneous alkaline earth metal compound nuclei. It is also reasonably speculated that the retention of the  $\text{M}\text{--}\text{O}$  bond would be present in the initial nucleation stage during the thermolysis of  $\text{M}(\text{CF}_3\text{COO})_2$  in mixed solvents, because the alkaline earth metal ions were inclined to be coordinated by the oxygen atoms. At the same time, highly reactive  $\text{F}^-$  ions were released from the solution due to cleavage of the  $\text{C}\text{--}\text{F}$  bond in  $\text{CF}_3\text{COO}^-$ . Subsequently, the  $\text{M}\text{--}\text{O}$  bond would be gradually fluorinated

### Scheme 1. Hypothesized Mechanism for the Formation of High-Quality $\text{MF}_2$ Nanocrystals from Trifluoroacetate Complex Precursors via Controlled Fluorination in Solution Phase



to form a  $\text{M}\text{--}\text{F}$  bond. As a result, subsequent replacement of the  $\text{M}\text{--}\text{O}$  bond with a  $\text{M}\text{--}\text{F}$  bond would lead to the formation of  $\text{MF}_2$  nuclei (Scheme 1).

As indicated by our experimental results, in OA/ODE, only  $\text{MF}_2$  nuclei were generated for the alkaline earth metal from  $\text{Mg}$  to  $\text{Sr}$ , while for  $\text{Ba}$ ,  $\text{BaF}_2$  and  $\text{BaO}$  nuclei coexisted (Table 1). This result suggested that the trend for the formation of  $\text{MF}_2$  nuclei was depressed along the alkaline earth metal series. Naturally, the lighter the alkaline earth metal, the easier  $\text{MF}_2$  nuclei formed, owing to the fact that the basicity of the alkaline earth metal oxide gradually increases along the alkaline earth metal series. With the as-formed nuclei of  $\text{MF}_2$  via the controlled fluorination in surfactant solutions, high-quality nanocrystals could be prepared by maintaining the balance between nucleation and growth stages.

**3.2. Nanocrystal Growth and Shape Evolution of  $\text{MF}_2$  Nanocrystals.** Normally, the crystal shape of inorganic nanocrystals is determined by several factors, including the crystalline phase of the nuclei, the selection of surfactants, and the competition between kinetic and thermodynamic growth regimes.<sup>9a,c</sup> Recently, many works have revealed that the 1D and 2D growth modes for the nanocrystals were attributed to the templating action of micellar structures formed by self-assembly of capping ligands, which is different from the selective adsorption of surfactant onto specific crystal planes.<sup>11</sup> In this work, only  $\text{MgF}_2$  has the tetragonal structure, which is anisotropic. Therefore, as expected, we obtained anisotropic  $\text{MgF}_2$  nanocrystals: 1D nanorods with a preferred growth direction along the  $\langle 001 \rangle$  direction. In contrast to the tetragonal  $\text{MgF}_2$  nanocrystals, for our  $\text{MF}_2$  ( $M = \text{Ca}, \text{Sr}$ ) nanocrystals, they are of cubic phase with no structural anisotropy. Considering the various shapes of as-obtained  $\text{MF}_2$  nanocrystals under different solvent compositions and the large ratio of length to diameter of  $\text{SrF}_2$  nanowires ( $(7.0 \pm 0.3) \text{ nm} \times (80.6 \pm 13) \text{ nm}$ ) (Figure 5d), we suggest that the as-observed 1D and 2D growth modes for the  $\text{MF}_2$  nanocrystals were attributed to the templating direction of micellar structures formed by self-assembly of capping ligands. This type of formation is similar to what has been predicted for the growth of fcc cubic  $\text{Au}$ ,  $\text{Ag}$ , and  $\text{FePt}$  nanocrystals.<sup>11c-f</sup>

This capping ligands micelle-directed growth mode is further evidenced by the controlled growth of  $\text{MF}_2$  nanocrystals under different solvent species. Herein, we take the  $\text{SrF}_2$  nanocrystals as an example to rationalize this postulation. At fixed concentration of precursor under the reaction temperature of 260 °C and

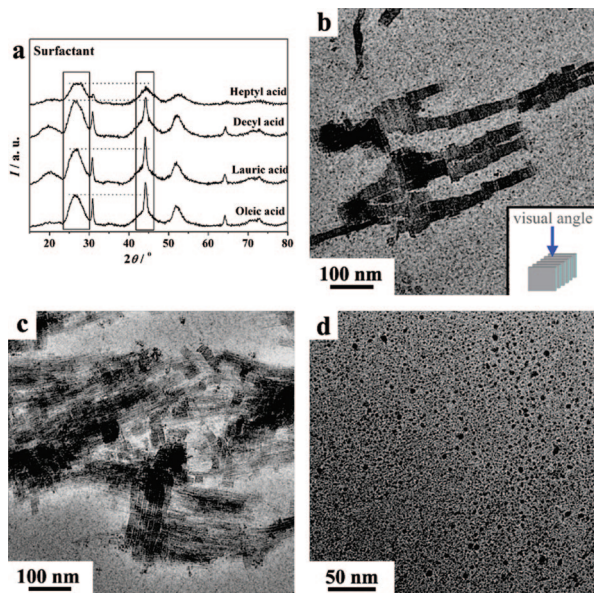


**Figure 8.** XRD patterns (a) and TEM images of  $\text{SrF}_2$  nanocrystals synthesized in different solvents: (a) lauric acid, (b) decyl acid, and (c) heptyl acid with the thermolysis of 1 mmol of  $\text{Sr}(\text{CF}_3\text{COO})_2$  at 260 °C for 60 min. (Inset) Schematic diagram of nanoplates.

the reaction time of 1 h, some fatty acids with different chain lengths such as lauric acid, decyl acid, and heptyl acid were employed to substitute for OA. As shown in the XRD patterns (Figure 8a), along with the decrease of the carbon chain length, the intensity of the (200) and (220) peaks declined, indicating that the anisotropic growth of the nanocrystals tended to be restrained. It could also be attested from the TEM images; the  $\text{SrF}_2$  nanoplates (Figure 8b) could be obtained by adopting lauric acid as the capping agent. The nanoplates containing nanowires were formed in the presence of decyl acid (Figure 8c), whereas only nonuniform nanoparticles were produced by employing heptyl acid as the capping ligand (Figure 8d). These results clearly suggest that various shapes of  $\text{MF}_2$  nanocrystals are likely obtained from the different micellar structures formed by self-assembly of the capping ligands, from which the polar groups attract to each other and the hydrophobic chains are intercalated to give the changeable channel structures (Scheme 1).

**4. Upconversion (UC) Emission Properties of  $\text{SrF}_2\text{:Yb,Er}$  and  $\text{SrF}_2\text{:Yb,Er@SrF}_2$  Nanocrystals.**  $\text{MF}_2$  is a well-known efficient host material for upconversion phosphors, which exhibits visible emission upon near-infrared (IR) excitation when doped with  $\text{Yb}^{3+}$  and  $\text{Er}^{3+}/\text{Tm}^{3+}$ .<sup>12</sup> By the developed current approach, we could also obtain high-quality rare earth-doped alkaline earth metal fluoride nanocrystals, using multiple metal trifluoroacetates as the precursors. Here, we choose  $\text{SrF}_2$  as a model host to study its upconversion properties by codoping with  $\text{Yb}^{3+}$  and  $\text{Er}^{3+}$  ions. TEM images in Figure 9a demonstrate that we obtained uniform  $\text{SrF}_2\text{:20%Yb,2%Er}$  nanosquares in the size of  $(13.7 \pm 1.0) \text{ nm} \times (18.9 \pm 1.5) \text{ nm}$ . Through manipulating the concept of “shell” on the nanocrystals surface, we can successfully get core/shell-structured  $\text{SrF}_2\text{:20%Yb,2%Er@SrF}_2$  nanocrystals, indicating the robustness and versatility of our synthetic method. Experimentally, the size of uniform  $\text{SrF}_2\text{:Yb,Er@SrF}_2$   $((15.7 \pm 1.5) \text{ nm} \times (19.3 \pm 1.3) \text{ nm})$  (Figure 9b) nanocrystals is larger than that of  $\text{SrF}_2\text{:Yb,Er}$  (Figure 9a). In addition, with the energy-dispersive X-ray spectra analysis (EDAX) (conducted at three different areas of the copper grid), the atomic ratio of Sr:Yb:Er is determined to be 4.60:1:0.07 for the core nanocrystals (Figure S7 in the Sup-

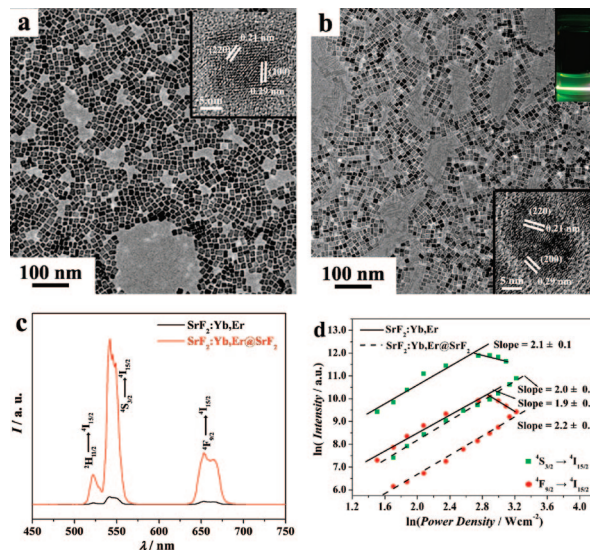


**Figure 9.** TEM images of the (a)  $\text{SrF}_2\text{:Yb,Er}$  and (b) core/shell-structured  $\text{SrF}_2\text{:Yb,Er@SrF}_2$  nanocrystals. (Inset) Eye-visible upconversion luminescence photograph of its solution. (c) Comparison of upconversion spectra of  $\text{SrF}_2\text{:Yb,Er}$  and  $\text{SrF}_2\text{:Yb,Er@SrF}_2$  nanocrystal dispersions in cyclohexane. (d) Power density dependence of the upconversion emission intensity for  $\text{SrF}_2\text{:Yb,Er}$  and  $\text{SrF}_2\text{:20%Yb,2%Er@SrF}_2$  nanocrystals under  $\lambda_{\text{ex}} = 980 \text{ nm}$ .

porting Information), close to the expected ratio (3.9:1:0.1), indicating the quantitative substitution of  $\text{Sr}^{2+}$  ions with the trivalent lanthanide cations in the  $\text{SrF}_2$  lattice. The atomic ratio of Sr:Yb:Er is determined to be 7.20:1:0.08 for the doped nanocrystals. The remarkable increase in the atomic ratio of Sr:Yb:Er after the core/shell treatment confirms the formation of the core/shell structure for the  $\text{SrF}_2\text{:Yb,Er@SrF}_2$  nanocrystals.<sup>13b,c</sup>

Figure 9c exhibits the room-temperature upconversion emission spectra of  $\text{SrF}_2\text{:20%Yb,2%Er}$  and  $\text{SrF}_2\text{:20%Yb,2%Er@SrF}_2$  nanoplates redispersed in cyclohexane under the 980 nm NIR excitation. The three characteristic emission bands centered at 525, 540, and 655 nm are observed, attributable to the  $^2\text{H}_{11/2}$  to  $^4\text{I}_{15/2}$ ,  $^4\text{S}_{3/2}$  to  $^4\text{I}_{15/2}$ , and  $^4\text{F}_{9/2}$  to  $^4\text{I}_{15/2}$  transitions of erbium, respectively. The emission efficiency of doped nanoparticles is usually lower than that of the corresponding bulk material as a result of the energy transfer process to the surface through adjacent dopant ions or the luminescence of surface dopant ions is quenched. As we have known, coating a shell made up of a material around the doped nanoparticles may enhance the emission of the phosphors greatly.<sup>13</sup> In this work, the formation of core/shell-structured  $\text{SrF}_2\text{:20%Yb,2%Er@SrF}_2$  enhances the intensity of green and red emissions compared with the  $\text{SrF}_2\text{:Yb,Er}$  core counterparts (the eye-visible luminescence photograph of  $\text{SrF}_2\text{:20%Yb,2%Er@SrF}_2$  was shown in the inset of Figure 9b).

In order to study the UC mechanism and determine the number of photons involved in the UC process of these nanocrystals, the intensities of the UC emissions are recorded as a function of the excitation density in log–log plots.<sup>14a</sup> The slopes for both the red and green curves are found to be approximately 2 (Figure 9d), indicating the two-photon absorption processes are involved in the UC behavior of the present nanocrystals.<sup>14</sup> Under the 980 nm laser excitation, the activated  $\text{Yb}^{3+}$  ion absorbs one photon and transfers it to the  $\text{Er}^{3+}$  ion, the  $\text{Er}^{3+}$  ion receives the energy and its ground-state  $^4\text{I}_{15/2}$  electron is excited to the  $^4\text{I}_{11/2}$  level, and the  $\text{Yb}^{3+}$  promotes  $\text{Er}^{3+}$  to  $^4\text{F}_{7/2}$  state via a nonradiative energy transfer process.



The excited electrons decay nonradiatively to  $^2H_{11/2}$ ,  $^4S_{3/2}$ , and  $^4F_{9/2}$  levels and precedently radiative relaxation to the ground state results in the emission of 525, 540, and 655 nm, respectively. At a high excitation density, the slope of the log–log curve is reduced due to the saturation of the UC processes. It can be seen that no obvious saturation is observed concerning the  $SrF_2:20\%Yb,2\%Er@SrF_2$  nanocrystals, and the saturation power is higher than that of  $SrF_2:20\%Yb,2\%Er$  nanocrystals for both green emission  $^4S_{3/2} \rightarrow ^4I_{15/2}$  (600 mW) and red emission  $^4F_{9/2} \rightarrow ^4I_{15/2}$  (576 mW), meaning the reduced nonradiative decays by decreasing the surface defects and the surface ligands influence for shell formation.<sup>13b,c</sup>

## Conclusions

Uniform alkaline earth fluoride  $MF_2$  ( $M = Mg, Ca, \text{ and } Sr$ ) nanocrystals with diverse shapes (tetragonal  $MgF_2$  nanoneedle-constructed 3D network; cubic  $CaF_2$  nanoplates and nanopolyhedra; cubic  $SrF_2$  nanoplates and nanowires) were synthesized from the thermolysis of  $M(CF_3COO)_2$  in hot surfactant solutions (oleic acid, oleylamine, and 1-octadecene). On the basis of a series of experiments by varying the experimental parameters, such as precursor concentration, solvent composition, reaction temperature, and time, the formation mechanism of these nanocrystals was proposed. For phase-pure  $MF_2$  nanocrystals, the growth of the shape-selective  $MF_2$  nanocrystals was likely due to the template direction of micellar structures formed by self-assembly of capping ligands and the so-called “Ostwald ripening” process. With the developed synthetic strategy, we also obtained the high-quality upconversion  $SrF_2:Yb,Er$  and core/shell  $SrF_2:Yb,Er@SrF_2$  nanocrystals. The core/shell-structured nanocrystals exhibited enhanced emission intensity and saturation power with respect to their core counterparts, owing to the suppression of associated nonradiative decays. The excellent optical properties of the as-synthesized nanocrystals demonstrate that they may become promising upconversion emission nanophosphors of adequate theoretical and practical interest.

**Acknowledgment.** We gratefully acknowledge the financial support from the MOST of China (grant no. 2006CB601104), the NSFC (grant nos. 20871006, 20821091, and 20671005).

**Supporting Information Available:** More results obtained by means of TEM, XRD, and EDAX for  $MF_2$  nanocrystals. This material is available free of charge via the Internet at <http://pubs.acs.org>.

## References

- (1) Nakajima, T.; Žemva, B.; Tressaud, A. *Advanced Inorganic Fluorides*; Elsevier: Amsterdam, 2000; Chapter 10.

- (2) (a) Singh, R.; Sinha, S.; Chou, P.; Hsu, N. J.; Radpour, F.; Ullal, H. S.; Nelson, A. J. *J. Appl. Phys.* **1989**, *66*, 6179. (b) Doualan, J. L.; Camy, P.; Moncorgé, R.; Daran, E.; Couchaud, M.; Ferrand, B. *J. Fluorine Chem.* **2007**, *128*, 459.
- (3) (a) Sata, N.; Eberman, K.; Eberl, K.; Maier, J. *Nature* **2000**, *408*, 946. (b) Sayle, D. C.; Doig, J. A.; Parker, S. C.; Watson, G. W. *Chem. Commun.* **2003**, 1804. (c) Maier, J. *Nat. Mater.* **2005**, *4*, 805. (d) Guo, X. X.; Matei, I.; Lee, J. S.; Maier, J. *Appl. Phys. Lett.* **2007**, *91*, 103102. (e) Kumar, G. A.; Chen, C. W.; Ballato, J.; Riman, R. E. *Chem. Mater.* **2007**, *19*, 1523. (f) Wang, F.; Liu, X. G. *J. Am. Chem. Soc.* **2008**, *130*, 5642.
- (4) (a) Sun, X. M.; Li, Y. D. *Chem. Commun.* **2003**, 1768. (b) Cao, M. H.; Hu, C. W.; Wang, E. B. *J. Am. Chem. Soc.* **2003**, *125*, 11196. (c) Lian, H. Z.; Liu, J.; Ye, Z. R.; Shi, C. S. *Chem. Phys. Lett.* **2004**, *386*, 291. (d) Feldmann, C.; Römig, M.; Trampert, K. *Small* **2006**, *2*, 1248. (e) Gao, P.; Xie, Y.; Li, Z. *Eur. J. Inorg. Chem.* **2006**, *16*, 3261. (f) Zhang, X. M.; Quan, Z. W.; Yang, J.; Yang, P. P.; Lian, H. Z.; Lin, J. *Nanotechnology* **2008**, *19*, 075603. (g) Quan, Z. W.; Yang, D. M.; Yang, P. P.; Zheng, X. M.; Lian, H. Z.; Liu, X. M.; Lin, J. *Inorg. Chem.* **2008**, *47*, 9509.
- (5) Roberts, J. E. *J. Am. Chem. Soc.* **1961**, *83*, 1087.
- (6) (a) Langford, J. I. *J. Appl. Crystallogr.* **1971**, *4*, 259. (b) Langford, J. I. *J. Appl. Crystallogr.* **1973**, *6*, 190.
- (7) (a) Smith, D. J.; Petford-Long, A. K.; Wallenberg, L. R.; Bovin, J. O. *Science* **1986**, *233*, 872. (b) Egerton, R. F.; Wang, F.; Crozier, P. A. *Microsc. Microanal.* **2006**, *12*, 65. (c) Latham, A. H.; Williams, M. E. *Langmuir* **2008**, *24*, 14195.
- (8) (a) Si, R.; Zhang, Y. W.; Zhou, H. P.; Sun, L. D.; Yan, C. H. *Chem. Mater.* **2007**, *19*, 18. (b) Sun, X.; Zhang, Y. W.; Du, Y. P.; Yan, Z. G.; Si, R.; You, L. P.; Yan, C. H. *Chem. Eur. J.* **2007**, *13*, 2320.
- (9) (a) Murray, C. B.; Kagan, C. R.; Bawendi, M. G. *Annu. Rev. Mater. Sci.* **2000**, *30*, 545. (b) Peng, Z. A.; Peng, X. G. *J. Am. Chem. Soc.* **2001**, *123*, 1389. (c) Peng, X. G. *Adv. Mater.* **2003**, *15*, 459. (d) Tao, A. R.; Habas, S.; Yang, P. D. *Small* **2008**, *4*, 310.
- (10) (a) Yin, Y. D.; Rioux, R. M.; Erdonmez, C. K.; Hughes, S.; Somorjai, G. A.; Alivisatos, A. P. *Science* **2004**, *304*, 711. (b) Kim, D.; Park, J.; An, K.; Yang, N.-K.; Park, J.-G.; Hyeon, T. *J. Am. Chem. Soc.* **2007**, *129*, 5812.
- (11) (a) Sun, Y.; Gates, B.; Mayers, B.; Xia, Y. *Nano Lett.* **2002**, *2*, 165. (b) Caswell, K. K.; Bender, C. M.; Murphy, C. J. *Nano Lett.* **2003**, *3*, 667. (c) Wang, C.; Hou, Y.; Kim, J.; Sun, S. *Angew. Chem., Int. Ed.* **2007**, *46*, 6333. (d) Lu, X. M.; Yavuz, M. S.; Tuan, H. Y.; Korgel, B. A.; Xia, Y. N. *J. Am. Chem. Soc.* **2008**, *130*, 8900. (e) Wang, C.; Hu, Y. J.; Lieber, C. M.; Sun, S. H. *J. Am. Chem. Soc.* **2008**, *130*, 8902. (f) Huo, Z. Y.; Tsung, C. K.; Huang, W. Y.; Zhang, X. F.; Yang, P. D. *Nano Lett.* **2008**, *8*, 2041.
- (12) (a) Bouffard, M.; Jouart, J. P.; Joubert, M. F. *Opt. Mater.* **2000**, *14*, 73. (b) Auzel, F. *Chem. Rev.* **2004**, *104*, 139. (c) Kishi, Y.; Tanabe, S.; Tochino, S.; Pezzotti, G. *J. Am. Ceram. Soc.* **2005**, *88*, 3423. (d) Bensalah, A.; Mortier, M.; Patriarche, G.; Gredin, P.; Vivien, D. *J. Solid State Chem.* **2006**, *179*, 2636. (e) Kumar, G. A.; Chen, C. W.; Riman, R. E. *Appl. Phys. Lett.* **2007**, *90*, 093123.
- (13) (a) Stouwdam, J. W.; van Veggel, F. C. J. M. *Nano Lett.* **2002**, *2*, 733. (b) Mai, H. X.; Zhang, Y. W.; Sun, L. D.; Yan, C. H. *J. Phys. Chem. C* **2007**, *111*, 13721. (c) Mai, H. X.; Zhang, Y. W.; Sun, L. D.; Yan, C. H. *J. Phys. Chem. C* **2007**, *111*, 13730.
- (14) (a) Scheps, R. *Prog. Quantum Electron.* **1996**, *20*, 271. (b) Du, Y. P.; Zhang, Y. W.; Sun, L. D.; Yan, C. H. *J. Phys. Chem. C* **2008**, *112*, 405.

CG801371R